Optical Power Monitoring with Ultrahigh Sensitivity in Silicon Waveguides and Ring Resonators
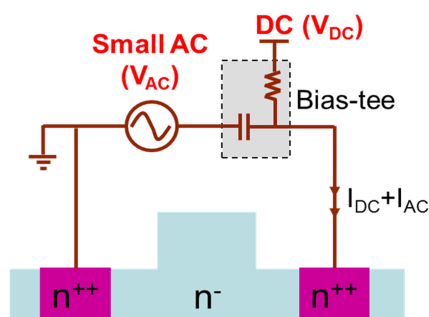
Dong Li
Linjie Zhou, *Member, IEEE*
Liangjun Lu
Jianping Chen

Optical power monitor using photoconductive effect in silicon waveguides

Optical Power Monitoring with Ultrahigh Sensitivity in Silicon Waveguides and Ring Resonators

Dong Li, Linjie Zhou, *Member, IEEE*, Liangjun Lu, and Jianping Chen

State Key Laboratory of Advanced Optical Communication Systems and Networks, Department of Electronic Engineering, Shanghai Jiao Tong University, Shanghai 200240, China

Abstract: We demonstrate optical power monitoring using a silicon resistor enabled by the surface and defect states-induced photoconductance effect. Ultrahigh optical power detection sensitivity of -40 dBm under a low AC drive voltage of 5 mV is obtained with the facilitation of a lock-in amplifier circuitry. The detection scheme is applied to monitor the resonances in single and coupled-ring resonators. Intracavity resonance spectrum is successfully measured at both the static and the thermal tuning conditions. The demonstration opens a compelling new way for nonintrusive on-chip optical power detection by exploiting doped silicon resistor-based thermooptic heaters.

Index Terms: Silicon nanophotonics, waveguide devices, Photodetectors, waveguides.

1. Introduction

In recent years, there has been significant progress on silicon photonics integration [1]–[4], which leverages the mature complementary metal-oxide-semiconductor (CMOS) fabrication processes for potential low-cost and high-volume production. As key components in photonic integrated circuits (PICs), photodetectors have attracted a lot of research interest and have been widely investigated. Germanium-based photodetectors show excellent performances in terms of compactness, responsibility, and bandwidth [5], [6]. However, the epitaxial growth of germanium on silicon is a non-trivial process, with great challenges in getting low-defect high-quality germanium thin films. III–V materials (such as InP and GaAs) can also be exploited to make high-efficiency photodetectors [7]–[9]. However, it imposes even greater challenges on the hybrid integration with silicon waveguides due to its intrinsic material incompatibility with silicon from the fabrication point of view.

Silicon has an indirect bandgap of 1.12 eV, higher than the photon energy of 0.8 eV in the 1550 nm optical communication band. It thus makes silicon an attractive material for low-loss optical wave guiding, but on the other hand, it also prohibits the realization of efficient photodetection in this wavelength band. Several all-silicon photodetection approaches have been proposed and demonstrated that can overcome the intrinsic limitation. For example, the middle bandgap state absorption (MSA), in which the generation of electron-hole pairs is mediated by the middle bandgap states generated from dedicated ion implantation, can greatly improve the absorption efficiency [10].

A responsivity of 87±29 mA/W with a dark current of <10 μA have been demonstrated in a Zn$^+$ implanted waveguide at mid-infrared wavelength [11]. The nonlinear effect such as two photon absorption (TPA) can also been used for photocarriers generation [12], [13], but it needs high optical power in the waveguide to allow appreciable photocurrent generation.

Other than MSA and TPA, there also exist weak absorption effects that can be used for sensing optical power in the silicon waveguides. These effects include surface state absorption (SSA) and defect state absorption (DSA). Similar to MSA, SSA allows an electron in the valence band to absorb one photon to reach the surface state and then absorb another photon to arrive at the conduction band. Although the efficiency of photon absorption is quite weak [14], SSA is a linear effect [15] and readily available in silicon nanowire waveguides [16]–[19]. No extra ion implantation steps are required as in MSA, which makes it quite attractive in PICs that demand in-line optical power monitoring yet without perturbing the normal device operation or incurring extra optical power loss. N-type and P-type ion implantation (such as boron and phosphorus) could result in photoactive crystal defects including divacancies and interstitial clusters in the silicon waveguide. The subsequent high temperature annealing could partially repair these defects, but there still remain some residual crystal defects. These small number of defects can mediate sub-bandgap defect state absorption (DSA) [20], [21]. Then the question that remains to ask is how to amplify the weak photocurrent signal to enable useful optical power detection.

So far, a lot of structures have been reported to best utilize the weak SSA and DSA. For example, A PN junction is embedded inside a ring resonator to harness the resonance enhancement effect [22]; interleaved PN junction increases the overlap between the junction depletion region and the surface states, leading to higher detection efficiency [23]; the silicon waveguide conductance change is detected using a capacitively coupled electrical circuit [24]; photonic crystal slow light waveguide is used to enhance the light interaction with the surface states, resulting in a higher responsivity and lower power consumption [25], [26]. The above improvements make the SSA and DSA effects an attractive way for optical power monitoring.

In this work, we demonstrate optical power monitoring by measuring the slight conductance change in silicon waveguides due to the presence of SSA and DSA effects [27]. A low-frequency sinusoidal voltage source is used to drive the silicon resistor and the current response is measured with the help of a high precision lock-in amplifier. Optical power as low as -40 dBm can be detected. The low drive voltage used for detection guarantees the normal operation of the device even under thermal tuning. This detection method points to new ways for monitoring optical power in multiple critical spots as long as silicon resistors are available.

2. Devices Under Test

Fig. 1 illustrates the silicon waveguide and microring resonators integrated with resistive heaters that we choose to demonstrate the in-line optical power monitoring. The waveguide width is 500 nm and the height is 220 nm. The etched depth is 160 nm with a 60-nm slab left. The waveguide is lightly doped with a doping concentration of 8×10^{16} cm^{-3} and the slab regions beside the waveguide are highly doped with a doping concentration of 10^{20} cm^{-3}. The highly-doped regions are separated from the waveguide edges by 0.8 μm. Ohmic contract is made between the aluminum metal wires and the two highly-doped regions. When light propagates in the silicon waveguide, free-carriers are generated due to the SSA and DSA effects which increase the waveguide conductance. Thereby, the current flowing through the waveguide experiences a slight change if it is driven by a fixed voltage source. To detect the small current change, we used a lock-in amplifier system in which the alternating current (AC) small-signal response was measured. An AC drive voltage with an amplitude of a few mV can produce high enough current. The small signal is advantageous as it avoids perturbation of the waveguide optical mode (phase in particular). It should be noted that during the optical power detection, the waveguide can still be thermally tuned using another direct current (DC) voltage source. The AC and DC voltages can be combined via a bias-tee as will be elaborated in the next section.
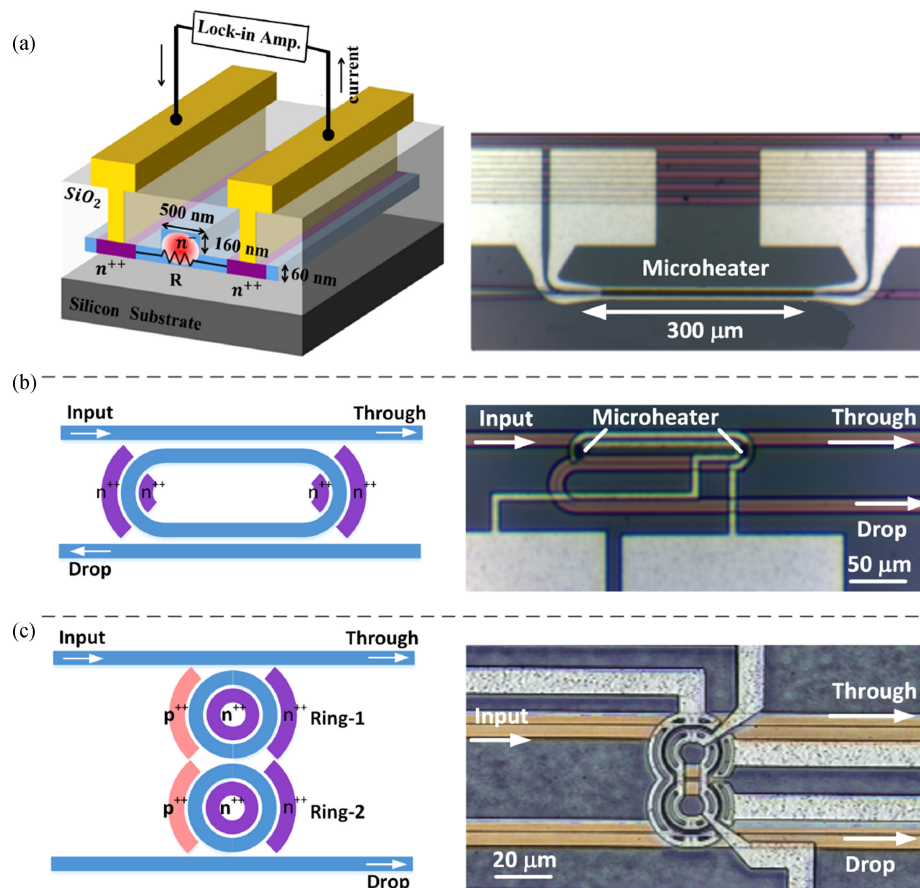
Fig. 1. Schematic structures and optical microscope images of three devices tested using our detection method: (a) silicon waveguide, (b) single-ring resonator, and (c) coupled-ring resonators. The AC detection signal is applied to the $n^{++}-n^{-}-n^{++}$ resistor embedded in the silicon waveguide.

3. Experiments and Results

3.1 Straight Waveguide

We first performed the optical power detection on a straight silicon waveguide as shown in Fig. 1(a). The active waveguide length is 300 μm. The waveguide propagation loss is around 3 dB/cm. As the optical mode is highly confined in the waveguide and not overlapped with the heavy doping regions, the doping induced excess loss is negligible. A sinusoidal voltage signal from a lock-in amplifier (Signal Recovery, Model 7280) was applied to the electrodes of the resistor. The current through the resistor was measured and amplified by the lock-in amplifier.

The magnitude and frequency of the AC driving signal influence the detection efficiency. Fig. 2(a) shows the measured current as a function of the AC driving signal frequency at various optical power levels in the waveguide. The AC voltage is fixed at 5 mV. The current response is flat in the low frequency end from 1 kHz to 30 kHz, but it decreases dramatically towards the high frequency end, which we attribute to the parasitic inductance in the electrical circuit. The photocurrent is defined as the difference between the total current (laser on) and the dark current (laser off). After subtracting the dark current, we obtained the photocurrent shown in Fig. 2(b). The measurement reveals that optical power as low as -40 dBm can be detected by the lock-in amplifier system. This minimum detectable optical power is limited by the noise level in the electric circuit. It could be further improved by using a more sensitive lock-in amplifier system or increasing the photoconductivity of the silicon waveguide under probe. The photoconductivity increases if the
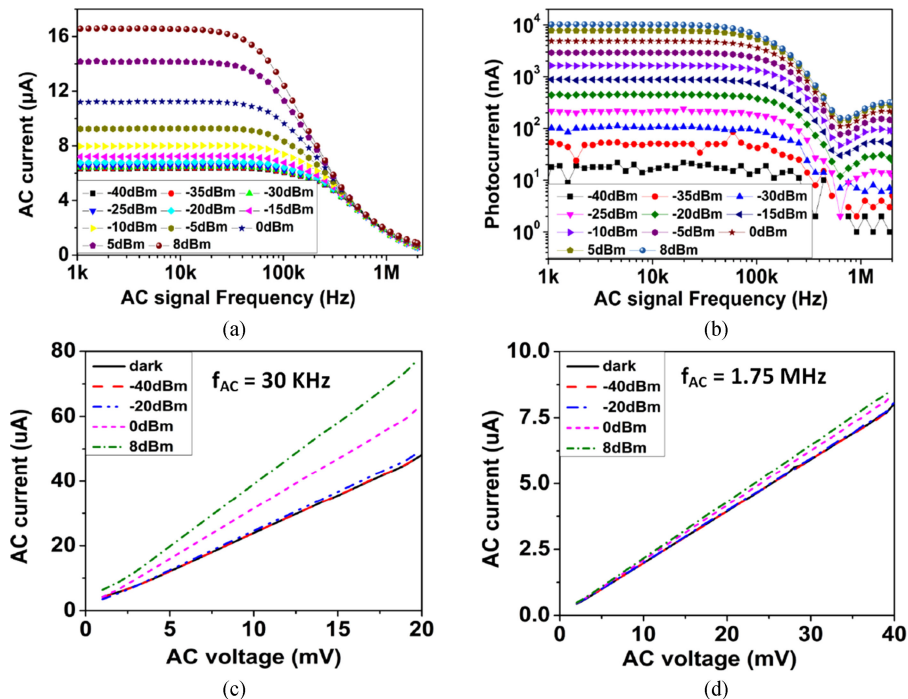
Fig. 2. Optical power monitoring in a silicon waveguide. (a) Measured AC current as a function of frequency at various optical powers. The AC voltage magnitude is fixed at 5 mV. (b) Extracted photocurrent as a function of frequency. (c) and (d) AC I-V curves at the signal frequencies of 30 kHz and 1.75 MHz.

silicon waveguide is unpassivated after etching off the upper cladding (enhancing SSA) or if the silicon waveguide is subject to ion implantation with incomplete lattice repair (enhancing DSA).

Fig. 2(c) and (d) show the linear dependence of the current on voltage at two frequencies: 30 kHz and 1.75 MHz. The slope reflects the small-signal conductance of the silicon resistor. Higher optical power increases the conductance due to the increased free carrier concentration by SSA and DSA. Comparing the curves at these two frequencies, one sees that at the lower frequency more significant current change is achieved.

As mentioned above, the DC and AC voltages can be simultaneously applied onto the resistor. The DC voltage is used to thermally tune the waveguide refractive index while the AC signal is used to sense the optical power. These two voltage sources are combined by a bias-tee, as sketched in Fig. 3(a). Fig. 3(b) shows the measured DC I-V curves under various optical powers. The nonlinearity of the I-V curves is due to the doping-induced junction behavior. In fact, there are two junctions at the interfaces between the lightly-doped and heavily-doped regions. The small-signal AC response is determined by the slope of the DC I-V curve. Therefore, the detected AC current is dependent on the DC bias voltage. At a small DC bias (e.g., 2 V), the AC current increases with the optical power; however, at a large DC bias (e.g., 6.5 V), the AC current decreases with the optical power. This abnormal phenomenon significantly affects the photocurrent detection, and therefore, calibration is required in order to correctly extract the optical power in the waveguide.

Fig. 4(a) shows the measured AC photocurrent changes as a function of DC voltage at various optical powers. Two distinct regimes can be clearly discerned. When the DC voltage is small (< 6 V), more photocurrent is detected with the increase of optical power. However, at a larger DC voltage (> 6 V), the photocurrent reduces with the increasing optical power. The negative value means the total AC current with light on is actually smaller than the dark AC current. This is consistent with the I-V curve measurement in Fig. 3(b). This measurement indicates that the presence of optical wave in the waveguide reduces (increases) the AC impedance at a low (high) DC bias.
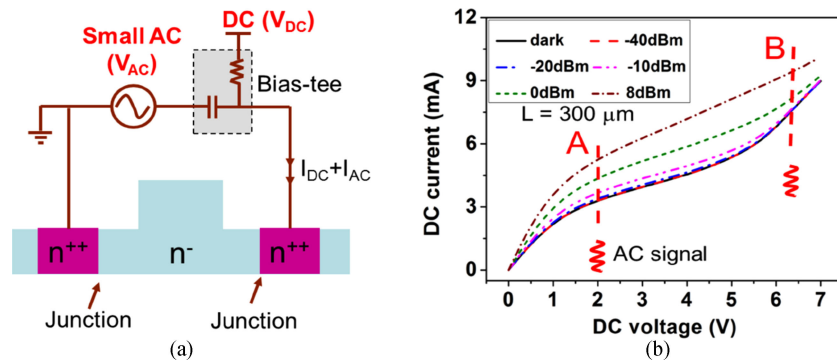
Fig. 3. (a) Circuit diagram showing the combined thermo-optic tuning and optical power detection in a straight waveguide. (b) Measured DC I-V curve in the waveguide under various optical powers. Note the slope change trend with increasing optical power is different at points A and B.
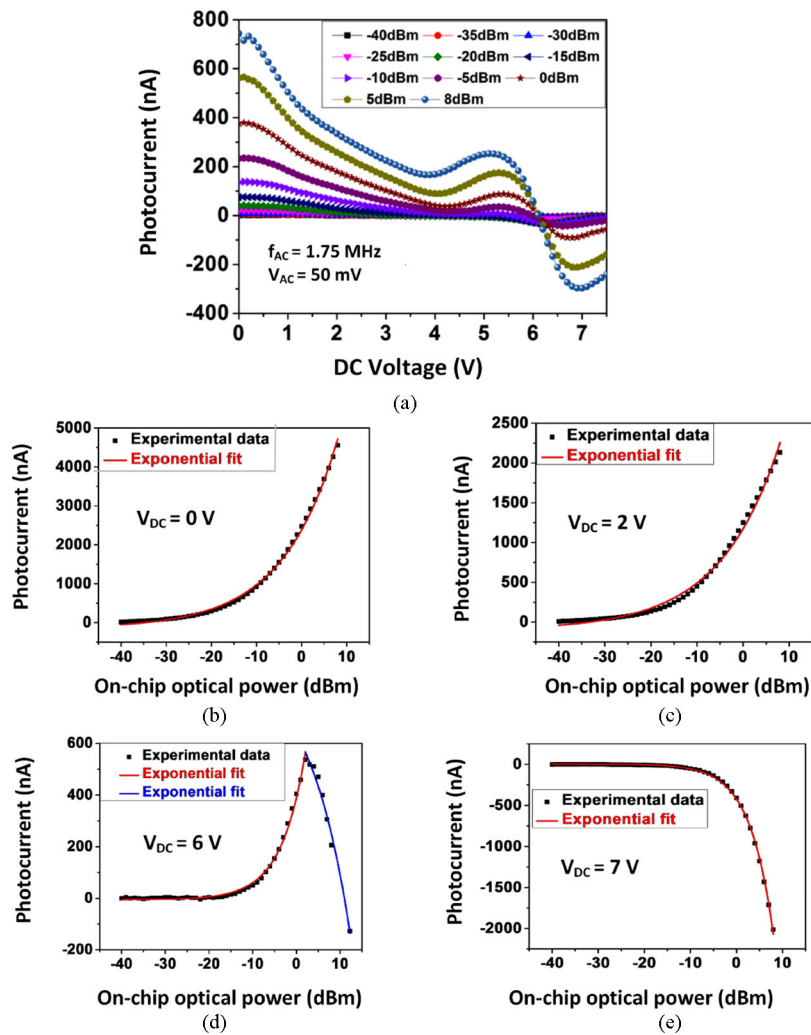

Fig. 4. (a) Photocurrent versus DC voltage at various optical powers. (b)–(e) Photocurrent changes as a function of on-chip optical power with the DC bias voltage at (b) 0 V, (c) 2 V, (d) 6 V, and (e) 7 V.
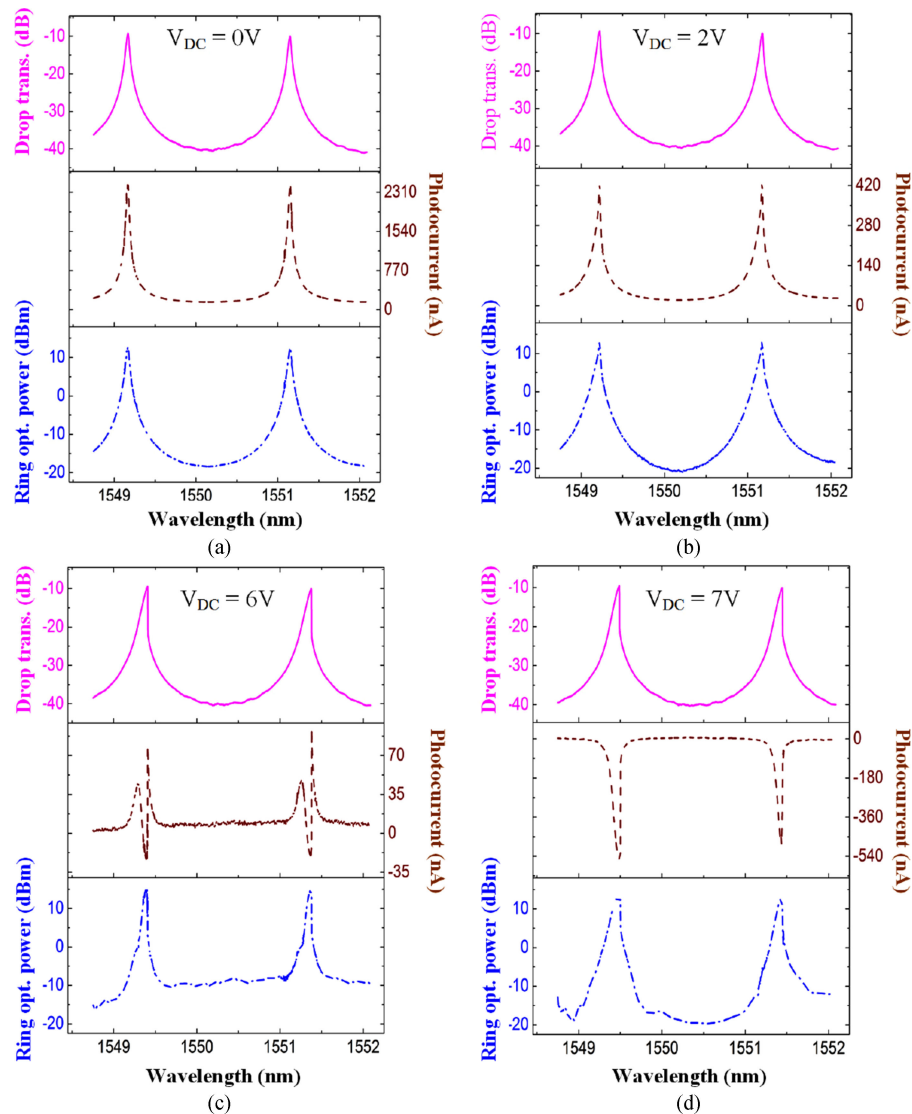
Fig. 5. Thermo-optic tuning and optical power detection in a single-ring resonator when the DC voltage is (a) 0 V, (b) 2 V, (c) 6 V and (d) 7 V.

Fig. 4(b)–(e) show the photocurrent changes with optical power. It can be seen that the DC voltage plays a significant role in the photocurrent curve. At low DC voltages of 0V and 2V, the photocurrent monotonously increases with optical power. At 6V, the photocurrent first increases and then decreases with optical power. At 7V, the photocurrent monotonously decreases with optical power. These curves are useful in extracting the optical power in the waveguide from the measured photocurrent at a certain DC voltage.

3.2 Single-Ring Resonator

We next performed the optical power measurement in a single-ring resonator with a Q-factor of $\sim 10^4$ using our detection method. The resistor is distributed in two curved sections of the ring resonator with a total length of $\sim 20~\mu$m. The ring resonance wavelength can be tuned by the DC voltage and the intra-cavity optical power can be simultaneously monitored using the AC signal. The optical power in the access waveguide is around 0 dBm. Fig. 5 shows the transmission spectrum at
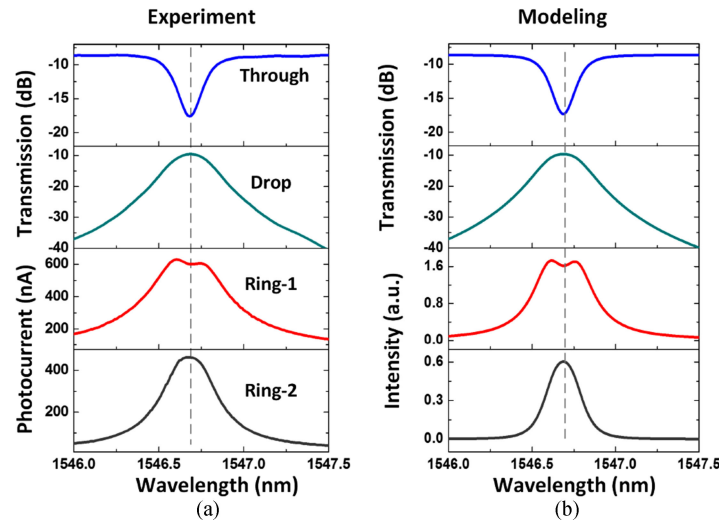
Fig. 6. (a) Measured optical transmission spectra and the corresponding photocurrent in the two ring resonators. (b) Modeled optical transmission spectra and the intensity in the two ring resonators. The dashed lines indicate the resonance wavelength.

the drop port for transverse electric (TE) polarization, the measured photocurrent, and the extracted optical power in the ring resonator at four different DC voltages. The frequency of the AC signal is 1.75 MHz and the amplitude is 50 mV. The monitored optical power in the ring resonator is still sensitive to the AC frequency, as in the straight waveguide case. Here we choose the same AC signal as that used in Fig. 4, so that the optical power can be extracted according to the calibration curves.

The optical power in the ring waveguide is greatly enhanced at resonance, and therefore the photocurrent increases rapidly close to the resonance wavelength. The drop transmission spectrum was measured by using a scanning laser method as shown in the first panel. The lock-in amplifier was then turned on to measure the photocurrent through the resistor. At low DC voltages (0V and 2V), the resonance peaks are well tracked in the photocurrent spectrum. The 2V DC tuning causes ~0.1 nm resonance wavelength shift. However, when the DC voltage increases to 6V, a notch appears at the resonance wavelength. This abnormality is originated from the decreasing of photocurrent at high optical power. At 7 V, because the photocurrent monotonically drops with the increasing optical power, the measured photocurrent spectrum exhibits a notch at the resonance wavelength. With the measured photocurrent versus optical power at various DC voltages (see Fig. 4), we can convert the photocurrent spectrum into the ring waveguide optical power spectrum, which overall well follows the drop spectrum. It illustrates the effectiveness of the optical power detection method in monitoring the single resonance. It should be noted that the slight asymmetric lineshape of the resonance spectrum is due to the enhanced nonlinear thermo-optic effect under resistive heating [28].

3.3 Coupled-Ring Resonators

Optical power detection in coupled-ring resonators has also been investigated using our detection scheme. The AC signal used for detection is the same with that in the single-ring resonator test. The device that we characterized is shown in Fig. 1(c), where two identical ring resonators are directly coupled. Each ring resonator is integrated with a p-i-n diode and a silicon resistive heater. Here we will demonstrate that the resistive heater can also be exploited to monitor the optical power in each ring resonator. The ring radius is 10 μm and the heater length is 18.5 μm.

The top two plots in Fig. 6(a) shows the measured through and drop spectra for TE polarization without thermal tuning. The bottom two plots present the photocurrent spectra in the two ring resonators. It is interesting to note that photocurrent peak around the resonance in the two rings are not identical. The top ring (ring-1) exhibits two overlapped peaks, making it look broader than that of the bottom ring (ring-2).

For the coupled ring resonators, the normalized field at the through and drop ports can be expressed in a recursive fashion using the optical field transfer matrix method. The bottom part of the device (including the inter-ring coupler, the bottom ring resonator and the output coupler) can be regarded as a complex coupler with the transmission and coupling coefficients being E_{tt} and E_{dd}, given by

$$E_{tt} = \frac{t_u - a_2 t_c e^{-i\phi_2}}{1 - a_2 t_u t_c e^{-i\phi_2}} \tag{1}$$

$$E_{dd} = \frac{-\kappa_u \kappa_c \sqrt{a_2} e^{-i\phi_2/2}}{1 - a_2 t_u t_c e^{-i\phi_2}} \tag{2}$$

where $t_c(\kappa_c)$ and $t_u(\kappa_u)$ are the optical field transmission (coupling) coefficients of the ring-waveguide and inter-ring couplers, respectively, ϕ_2 is the round-trip phase change in the bottom ring resonator, and a_2 is the loss factor of the bottom ring. The electric field at the through and drop ports of the coupled-ring resonators are then expressed as

$$E_t = \frac{t_c - a_1 E_{tt} e^{-i\phi_1}}{1 - t_c a_1 E_{tt} e^{-i\phi_1}} \tag{3}$$

$$E_d = \frac{-i\kappa_c \sqrt{a_1} E_{dd} e^{-i\phi_1/2}}{1 - t_c a_1 E_{tt} e^{-i\phi_1}} \tag{4}$$

where ϕ_1 and a_1 are the round-trip phase change and loss factor of the top ring resonator, respectively. The optical intensity in the two ring resonators are related to E_t and E_d as (assuming weak coupling, $t_c \sim 1$)

$$I_{r1} \approx \frac{|1 - E_t|^2}{\kappa_c^2} \tag{5}$$

$$I_{r2} \approx \frac{|E_d|^2}{\kappa_c^2} \tag{6}$$

The parameters t_c, t_u, a_1, a_2 are obtained by fitting the measured spectra using (3) and (4). The optical intensity in the two rings can then be derived using (5) and (6) as shown in Fig. 6(b). Comparing the measured photocurrent and modeled intensity spectra, we see that they agree well qualitatively. The good match approves the validity and reliability of our optical power monitoring method in the coupled-ring resonators. The dual-peak feature in the ring-1 photocurrent curve is due to the large phase change of E_t across resonance implied by (5). The photocurrent in the ring-2 always follows the drop spectrum as suggested by (6).

As we highlighted previously that the key merit of our optical power detection scheme is that it reuses the resistive heater without affecting the normal thermal tuning function. Fig. 7 presents the measurement results when one of the rings (ring-1) is thermally tuned at 1V and 4V DC voltages. With the resonances of the two rings gradually separated, the through (drop) spectrum shows a broader stopband (passband). The photocurrent measurement reveals this trend. It is noted that the photocurrent spectra from both rings are broadened at 4 V DC voltage as the first ring resonance deviates far apart from the second one.

The resonances from the two ring resonators are directly coupled to generate the second-order filtering profile. The coupling between the two resonators can be understood from the coupled mode theory. The coupling between the two resonators leads to symmetric and anti-symmetric resonance super-modes, which broadens the through and drop transmission spectra. With increased wavelength detuning between the individual resonances, the super-modes are gradually degraded
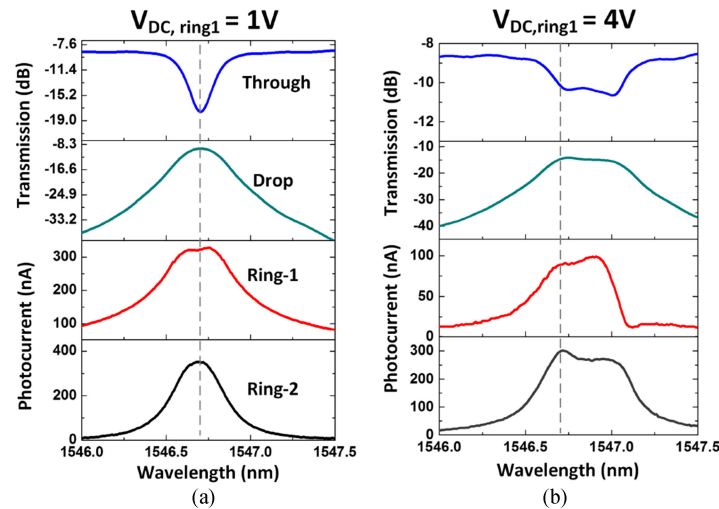
Fig. 7. Measured optical transmission spectra and the corresponding photocurrent in the two ring resonators when ring-1 is thermally tuned with a DC voltage of (a) 1V and (b) 4V. The dashed lines indicate the original resonance wavelength.

into the individual modes. Therefore, the Ring-1 photocurrent spectrum has a peak raised towards the right side, given by the red-shifted Ring-1 resonance, while the Ring-2 photocurrent spectrum has the peak raised at the original resonance wavelength governed by the un-shifted Ring-2 resonance. This explains the measured asymmetric photocurrent spectrum in Fig. 7(b). The results presented here lead to new possibilities for directly measuring the intra-cavity optical intensity, which is otherwise impossible to access from the input/output waveguide ports.

Our detection technique is similar to the contactless integrated photonic probe (CLIPP) [24] in that they both rely on the light-induced silicon waveguide conductance change. However, there are still certain differences in the extraction method for the small conductance or current variation. The CLIPP technique exploits a capacitive access to the waveguide, which increases the total impedance of electric circuit. This may lower the detection sensitivity. The measured sensitivity is -30 dBm under a drive voltage of 1V at 1 to 2 MHz frequency. In our scheme, however, the external AC signal directly drives the silicon resistor, leading to an improved sensitivity of -40 dBm. Moreover, the drive voltage amplitude used for ring resonator test is only 50 mV, 20 times smaller than that used in CLIPP. The low drive voltage is advantageous as it brings negligible perturbation to the light propagating in the waveguide.

4. Conclusion

We have demonstrated optical power monitoring in silicon waveguides and ring resonators using the surface and defect states-induced photoconductance effect. The detection utilizes the existing resistive heaters integrated in thermally tunable devices. It is non-invasive in that waveguide mode is not perturbed and thermal tuning can still be performed as normal. The minimum detectable optical power can be as low as -40 dBm with a low drive voltage of only 5 mV. Due to the junction behavior of the silicon resistors, its I-V response is nonlinear, rendering the small-signal photocurrent significantly dependent on DC voltage and optical power. The intra-cavity resonance spectrum can be correctly retrieved, which can be used to track resonance wavelengths. The detection scheme is also applicable to more complicated coupled resonators so that the optical intensity inside each resonator can be directly monitored. The silicon resistor-based detection scheme could offer a route to powerful detection and analysis of the constituent components in complex photonic circuits.

References

[1] G. Carpintero *et al.*, "Microwave photonic integrated circuits for millimeter-wave wireless communications," *J. Lightw. Technol.*, vol. 32, no. 2, pp. 3495–3501, Oct. 2014.

[2] T. Komljenovic *et al.*, "Heterogeneous silicon photonic integrated circuits," *J. Lightw. Technol.*, vol. 34, no. 1, pp. 20–35, Jan. 2016.

[3] J.-F. Song *et al.*, "Silicon photonic integrated circuits with electrically programmable non-volatile memory functions," *Opt. Exp.*, vol. 24, pp. 21744–21751, 2016.

[4] C. Sun *et al.*, "Single-chip microprocessor that communicates directly using light," *Nature*, vol. 528, pp. 534–538, 2015.

[5] S. Lischke *et al.*, "High bandwidth, high responsivity waveguide-coupled germanium pin photodiode," *Opt. Exp.*, vol. 23, pp. 27213–27220, 2015.

[6] H. Chen *et al.*, "–1 V bias 67 GHz bandwidth Si-contacted germanium waveguide pin photodetector for optical links at 56 Gbps and beyond," *Opt. Exp.*, vol. 24, pp. 4622–4631, 2016.

[7] K. Nozaki, S. Matsuo, K. Takeda, T. Sato, E. Kuramochi, and M. Notomi, "InGaAs nano-photodetectors based on photonic crystal waveguide including ultracompact buried heterostructure," *Opt. Exp.*, vol. 21, pp. 19022–19028, 2013.

[8] S. Feng, Y. Geng, K. M. Lau, and A. W. Poon, "Epitaxial III-V-on-silicon waveguide butt-coupled photodetectors," *Opt. Lett.*, vol. 37, pp. 4035–4037, 2012.

[9] L. Shen *et al.*, "High-bandwidth uni-traveling carrier waveguide photodetector on an InP-membrane-on-silicon platform," *Opt. Exp.*, vol. 24, pp. 8290–8301, 2016.

[10] D. F. Logan, P. E. Jessop, and A. P. Knights, "Modeling defect enhanced detection at 1550 nm in integrated silicon waveguide photodetectors," *J. Lightw. Technol.*, vol. 27, no. 7, pp. 930–937, Apr. 2009.

[11] R. R. Grote *et al.*, "Extrinsic photodiodes for integrated mid-infrared silicon photonics," *Optica*, vol. 1, pp. 264–267, 2014.

[12] H. Chen and A. W. Poon, "Two-photon absorption photocurrent in pin diode embedded silicon microdisk resonators," *Appl. Phys. Lett.*, vol. 96, 2010, Art. no. 191106.

[13] H. Zhu, L. Zhou, R. Yang, X. Li, and J. Chen, "Enhanced near-infrared photodetection with avalanche gain in silicon microdisk resonators integrated with pn diodes," *Opt. Lett.*, vol. 39, pp. 4525–4528, 2014.

[14] G. Chiarotti, S. Nannarone, R. Pastore, and P. Chiaradia, "Optical absorption of surface states in ultrahigh vacuum cleaved (111) surfaces of Ge and Si," *Phys. Rev. B*, vol. 4, pp. 3398–3402, 1971.

[15] T. Baehr-Jones, M. Hochberg, and A. Scherer, "Photodetection in silicon beyond the band edge with surface states," *Opt. Exp.*, vol. 16, pp. 1659–1668, 2008.

[16] S. Kar and S. Varma, "Determination of silicon–silicon dioxide interface state properties from admittance measurements under illumination," *J. Appl. Phys.*, vol. 58, pp. 4256–4266, 1985.

[17] L. Zhou, H. Zhu, H. Zhang, and J. Chen, "Photoconductive effect on pip micro-heaters integrated in silicon microring resonators," *Opt. Exp.*, vol. 22, pp. 2141–2149, 2014.

[18] Y. Li and A. W. Poon, "Actively stabilized silicon microrings with integrated surface-state-absorption photodetectors using a slope-detection method," *Opt. Exp.*, vol. 24, pp. 21286–21300, 2016.

[19] J. J. Ackert, A. S. Karar, J. C. Cartledge, P. E. Jessop, and A. P. Knights, "Monolithic silicon waveguide photodiode utilizing surface-state absorption and operating at 10 Gb/s," *Opt. Exp.*, vol. 22, pp. 10710–10715, 2014.

[20] H. Jayatilleka *et al.*, "Wavelength tuning and stabilization of microring-based filters using silicon in-resonator photoconductive heaters," *Opt. Exp.*, vol. 23, pp. 25084–25097, 2015.

[21] H. Yu *et al.*, "Using carrier-depletion silicon modulators for optical power monitoring," *Opt. Lett.*, vol. 37, pp. 4681–4683, 2012.

[22] Y. Li, S. Feng, Y. Zhang, and A. W. Poon, "Sub-bandgap linear-absorption-based photodetectors in avalanche mode in PN-diode-integrated silicon microring resonators," *Opt. Lett.*, vol. 38, pp. 5200–5203, 2013.

[23] H. Zhu, L. Zhou, X. Sun, Y. Zhou, X. Li, and J. Chen, "On-chip optical power monitor using periodically interleaved PN junctions integrated on a silicon waveguide," *IEEE J. Sel. Topics Quantum Electron.*, vol. 20, no. 4, pp. 56–63, Jul./Aug. 2014.

[24] F. Morichetti *et al.*, "Non-invasive on-chip light observation by contactless waveguide conductivity monitoring," *IEEE J. Sel. Topics Quantum Electron.*, vol. 20, no. 4, pp. 292–301, Jul./ Aug. 2014.

[25] Y. Terada, K. Miyasaka, H. Ito, and T. Baba, "Slow-light effect in a silicon photonic crystal waveguide as a sub-bandgap photodiode," *Opt. Lett.*, vol. 41, pp. 289–292, 2016.

[26] Z. Gu, T. Hiratani, T. Amemiya, N. Nishiyama, and S. Arai, "Study of a slow-light-enhanced membrane photodetector for realizing on-chip interconnection with low power consumption," *J. Optical Soc. Amer. B*, vol. 34, pp. 440–446, 2017.

[27] D. Li, L. Zhou, and J. Chen, "Ultrahigh-sensitivity on-chip power monitor using a resistive microheater in a silicon waveguide," in *Proc. IEEE 13th Int. Conf. Group IV Photon.*, 2016, pp. 16–17.

[28] L. Lu, L. Zhou, X. Li, and J. Chen, "Enhanced nonlinear thermo-optic effect in silicon microring resonators with pip microheaters for non-reciprocal transmission," in *Proc. Opt. Fiber Commun. Conf.*, 2014, Paper Th2A. 27.